A method to estimate reflection and directional spread using rotary spectra from accelerometers on large ice floes

Graig Sutherland*, Jean Rabault and Atle Jensen

Department of Mathematics, University of Oslo, Norway

**Corresponding author address:* Department of Mathematics, University of Oslo, Postboks 1053 Blindern, 0316 Oslo, Norway

E-mail: graigors@math.uio.no

ABSTRACT

The directional wave spectra in sea ice are an important aspect of the wave evolution and can provide insights into the dominant components of wave dissipation, i.e. dissipation due to scattering or dissipation due to viscous processes under the ice. In this paper we propose a robust method for the measurement of directional wave spectra parameters in sea ice from a 3-axis accelerometer or a heave, pitch and roll sensor. Our method takes advantage of certain aspects of sea ice and makes use of rotary spectra techniques to provide model-free estimates for the mean wave direction, directional spread and reflection coefficient. The method is ideally suited for large ice floes, i.e. where the ice floe length scale is much greater than the wavelength, but a framework is provided to expand the parameter space where the method may be effective.

1. Introduction

It has been common practice to use accelerometers, or inertial motion units (IMUs), to detect surface wave motion in sea ice (e.g. Wadhams et al. 1986). These have several advantages as they are low-cost, relatively easy to deploy, and there exists extensive literature on using such sensors for measuring ocean waves (Bender III et al. 2010). While techniques to obtain one-dimensional estimates of the wave energy are relatively robust (Bender III et al. 2010), there are several challenges associated with calculated directional wave spectra from a single sensor (Benoit 1992; Young 1994). One of the largest challenges for measuring waves in ice is due to the multimodal nature expected from reflections, scattering from inhomogeneities in the ice cover and changes in the dispersion relation (Wadhams et al. 1986; Sutherland and Rabault 2016).

Understanding the directional spectra is important in order to address the dominant mechanism for wave attenuation, which is due to the scattering of wave energy arising from inhomogeneity in the ice cover or due to viscous attenuation between the ice cover and the fluid beneath (Squire et al. 1995; Squire 2007). While both methods are expected to give an exponential amplitude decay as a function of distance (Wadhams et al. 1988), distinction between the two dissipative processes is expected to be possible if accurate measurements of the directional spread are available (Ardhuin et al. 2016). This is true for pack ice as well as the MIZ, as Ardhuin et al. (2016) used observations located between 1000-1500 km from the ice edge to infer the dissipation mechanism for waves with a period greater than 19 s.

The only published in situ study of the directional wave spectra in sea ice, to our knowledge (and according to Squire and Montiel (2016)), is the study by Wadhams et al. (1986) who used several heave, pitch and roll buoys to calculate the spectra inside and outside the marginal ice zone. Wadhams et al. (1986) calculated directional spectra using the methodology of Long and

Hasselmann (1979), which is an inverse technique that fits the observations to a preferred parametric model for the shape of the directional spectra, as this method has been shown to resolve bimodal seas (Lawson and Long 1983). There are other methodologies for calculating the directional spectra in bimodal seas, but they all require knowledge of the directional shape function and use various techniques to obtain the best fit (see Benoit (1992) for a review of some of the techniques). As a first approach we will make no assumptions about the spectral shape and will work directly with the Fourier series expansion approach of Longuet-Higgins et al. (1963). This approach is used in part to simplify the analysis, but is also justified due to the scarcity of observations of directional spectra in ice and the lack of data with regards to a preferred spreading shape. Recent advances in the development of low-cost IMUs have allowed for the development of wave sensors that can be developed into wave buoys or easily deployed on ice floes (e.g. Doble and Wadhams 2006; Kohout et al. 2015; Rabault et al. 2016). This development will make it easier to measure waves in ice and, therefore, greatly increase the number of in situ observations available. In addition, as these sensors can take advantage of satellite communications, such as Iridium, to send data remotely it is advantageous to be able to estimate aspects of the directional spectra in a robust manner, similar to the model-independent parameters proposed by Kuik et al. (1988), to reduce data transmission volume.

One of the primary motivations for this paper is to explain why the horizontal acceleration, as measured by an IMU on sea ice presented by Sutherland and Rabault (2016) and Rabault et al. (2016), is equivalent in magnitude to the vertical acceleration. In previous studies where the horizontal acceleration was presented (Fox and Haskell 2001; Bender III et al. 2010), the acceleration orthogonal to the vertical was shown to be negligible. The studies of Sutherland and Rabault (2016) and Rabault et al. (2016) intuitively used this information to infer the direction of propagation, but lacked a thorough analysis as to why this should be so. In this paper, a new methodology for estimating information about the directional spectra is presented. This method takes advantage of typical IMU measurements in order to obtain robust estimates of mean direction, directional spread, and reflection. These directional parameters are estimated using a rotary spectra technique (Gonella 1972). This technique is compared with that of Longuet-Higgins et al. (1963) as well as model-independent estimates using the Fourier coefficients (Kuik et al. 1988). The outline of the paper is as follows. Section 2 outlines the theoretical basis for our methodology and how it relates to the original theory as laid out by Longuet-Higgins et al. (1963). The data and methodology is presented in section 3. Details of the wave motion as measured by IMUs are presented in section 4. Calculation of directional spectra using an IMU and comparisons with the new rotary spectra method, along with estimating model-independent parameters for directional spread and reflection, is presented in 5. A summary and discussion of the results, along with limitations of the proposed method, can be found in section 6.

2. Theory

We begin our analysis with the three orthogonal accelerations in the reference frame of the IMU, as shown by Bender III et al. (2010) to be written as

$$X_S = a_x + g_x \tag{1}$$

$$Y_S = a_y + g_y \tag{2}$$

$$Z_S = a_z + g_z, \tag{3}$$

where a_x, a_y and a_z are the orthogonal accelerations and g_x, g_y and g_z are the components of gravity in the x, y and z directions of the IMU frame of reference, which we denote by the subscript S. There exists some variability in the coordinate system used by various IMU manufacturers (Bender III et al. 2010), but for our purposes we will use the VN-100 manufactured by VectorNav

(2014) and the orientation is shown in Figure 1. The components of gravity in each of the three orthogonal components are a function of the pitch θ, defined to be the angle rotated about the y axis in a right hand system, and ϕ, defined to be the angle rotated about the x axis in a right hand system, such that

$$g_x = g \sin\theta \tag{4}$$

$$g_y = -g \cos\theta \sin\phi \tag{5}$$

$$g_z = -g \cos\theta \cos\phi. \tag{6}$$

Equations (4)-(6) are identical to Method IV of Bender III et al. (2010).

Up to this point there has been no assumption made about the nature of the sea ice cover at the surface. For waves in sea ice, the ratio of the horizontal dimension of the ice floe to the wavelength is an important parameter determining the accelerations and angles of the ice floe relative to the ocean surface (Masson and LeBlond 1989; Meylan and Squire 1994). For ice floes much smaller than the wavelength, the response amplitude operator (RAO) of an ice floe to surface waves is controlled by gravity - i.e. the floe can slide down wave slopes - friction between the floe and water and inertia of the floe (Marchenko 1999). For wavelengths comparable to the ice floe length scale there can exist complex resonance characteristics strongly affecting the RAO (Masson and LeBlond 1989). For wavelengths much smaller than the ice floe, the ice floe will follow the waves under the ice and the flexural motion of the ice can change the dispersion relation. In general, the accelerations and angles in the three directions are functions of the incident wavelength, the floe geometry and to a small extent the water depth (Masson and LeBlond 1989). Below we will make some assumptions consistent with the conditions encountered by Sutherland and Rabault (2016), but note that the method may still work for smaller floes. This latter point will be elaborated on further in Section 6.

As one of the primary motivations for this study is to explain the horizontal accelerations observed by an IMU on a large continuous sheet of ice (Sutherland and Rabault 2016), we will make the assumption that the horizontal length scale of the ice floe is much greater than the wavelength. This assumption allows us to further assume that the ice is well coupled with the surface waves, i.e. that the horizontal motion is negligible $a_x = a_y = 0$, and that the angles θ and ϕ are small enough to neglect the second order terms, e.g.. $\sin\theta \approx \theta$ and $\cos\theta \approx 1$. These assumptions, along with (4)-(6), allow (1)-(3) to be written as

$$X_S = g\theta \tag{7}$$

$$Y_S = -g\phi \tag{8}$$

$$Z_S = a_Z - g. \tag{9}$$

Equations (7)-(9) show that a 3-D arrangement of accelerometers on sea ice, to first order, can measure the vertical acceleration along with the angles given the above assumptions. This is explored further for gravity waves propagating in sea ice.

The surface elevation can be written as

$$\eta(\mathbf{x},t) = \Re\left[Ae^{i(\mathbf{k}\cdot\mathbf{x}-\omega t)}\right] = \Re\left[Ae^{i\Phi}\right], \tag{10}$$

where $\Re$ denotes the real part, A is the amplitude, $\mathbf{k}$ is the wavenumber vector, ω is the angular frequency, $\mathbf{x}$ is the position vector, t is time and $\Phi = \mathbf{k}\cdot\mathbf{x} - \omega t$ is the phase function. While (10) is the elevation for a single frequency, it can easily be written as a linear sum of several frequencies with no loss of generality. The angles θ and ϕ are related to the slopes in the x and y directions and can be calculated from (10), i.e.

$$\theta = \frac{\partial \eta}{\partial x} = ik_x Ae^{i\Phi} \tag{11}$$

$$-\phi = \frac{\partial \eta}{\partial y} = ik_y Ae^{i\Phi}. \tag{12}$$

The vertical acceleration in our coordinate system, where z is positive downwards, is calculated as

$$a_z = -\frac{\partial^2 \eta}{\partial t^2} = \omega^2 A e^{i\Phi}. \tag{13}$$

The dispersion relation, assuming a Kirchoff-Love thin elastic plate model (Marchenko et al. 2013), can be written as

$$\omega^2 = gk \tanh(kH) \left(1 + \frac{D}{\rho g} k^4\right), \tag{14}$$

where $k = |\mathbf{k}| = \sqrt{k_x^2 + k_y^2}$, k_x and k_y are the orthogonal components of the wavenumber vector $\mathbf{k}$, $D = Eh^3 / \left[12\left(1 - \nu^2\right)\right]$ is the bending modulus with E being the elastic modulus of ice, H is the water depth, h is the ice thickness, ρ is the water density and ν is the Poisson ratio. We define a characteristic length scale for the flexural term identical to Fox et al. (2001), i.e.

$$\ell_c = \left(\frac{D}{\rho g}\right)^{1/4}. \tag{15}$$

There are other factors which can affect wave dispersion, such as the inertia of the ice and compressive stress (Liu and Mollo-Christensen 1988). However, ice stresses in an adjacent fjord have a maximum of 37.7 kPa away from the hinge zone (Vindegg 2014) , which are much too small to affect the dispersion for typical surface wave frequencies. The inertial term may affect the higher wavenumbers, but will be limited to a maximum 10% deviation in the dispersion relation for wavelengths less than 50 m and ice thicknesses less than 1 m, and is therefore neglected.

The wavenumber k can be written in terms of one of the orthogonal components k_x and k_y as

$$k = k_x \left(1 + \left(\frac{k_y}{k_x}\right)^2\right)^{1/2}. \tag{16}$$

In general, at least for lower frequencies which do not quickly attenuate, waves in ice can be approximated as long-crested, i.e. $(k_y/k_x)^2 \ll 1$ (Sutherland and Rabault 2016). Therefore, from (16), $k_x \approx k$ and k_y will be a small fraction of k. If we define $\delta k = k - k_y$, and solving for k such that $k_y = \varepsilon k$ and ignoring terms of δk^2 gives $\varepsilon = (2\delta k/k)^{1/2}$. Substituting (11)-(15) into (7)-(9)

gives

$$X_S = \frac{i\omega^2 A e^{i\Phi}}{\tanh kH \left[1 + (k\ell_c)^4\right]} \tag{17}$$

$$Y_S = \frac{\varepsilon i\omega^2 A e^{i\Phi}}{\tanh kH \left[1 + (k\ell_c)^4\right]} \tag{18}$$

$$Z_S = \omega^2 A e^{i\Phi} - g. \tag{19}$$

Equations (17)-(19) show that the magnitude of X_S will be comparable to Z_S with a 90° phase shift for wavenumbers $(k\ell_c)^4 \ll 1$. For Y_S, the same 90° phase shift is expected but with a much reduced amplitude.

The characteristic length for a range of elastic modulus E of $1-5\times 10^9$ N m^{-2} and ice thickness h of 0.5 to 1 m, gives a range for ℓ_c between 0.58 m and 14.6 m. For ocean swell where $(k\ell_c)^4 \ll 1$, the bending term can be omitted and X_S and Z_S should have the same magnitude. For thick, stiffer ice, the flexural motion will impact higher frequencies of wave motion, but for thin, more pliable ice the bending term in the dispersion relation can safely be neglected.

The finite depth can also lead to an increase in the measured horizontal acceleration X_S relative to the vertical acceleration Z_S for small values of kH. Taking H = 80 m, which is the depth for Sutherland and Rabault (2016), gives an increase of X_S relative to Z_S of 0.5% for wavelengths of 168 m, corresponding to waves with periods greater than 10 s, and 3.7% for wavelengths of 251 m, corresponding to waves with periods greater than 13 s. For H = 160 m, which is the depth for the other data which we will present later, the periods of 18 s and 15 s correspond to the 0.5% and 3.7% errors respectively.

Equations (17)-(19), bring up an interesting corollary with regards to when the magnitude of X_S is not equal to Z_S (e.g. Fox and Haskell 2001) or when X_S and Z_S are not 90° out of phase (e.g. Sutherland and Rabault 2016). Such an inequality could arise from physical horizontal motion (i.e. surge), flexural motion (i.e. $(k\ell_c)^4 \gg 1$), floe-floe interactions (Yiew et al. 2016) or the waves are not sufficiently long-crested (e.g. $|X_S| \approx |Y_S|$). Therefore, the accelerations measured in the IMU reference frame can give information about wave propagation when $|Z_S| \approx |X_S|$ and Z_S and X_S are 90° out of phase. The method can also potentially give some information about the ice cover when only a subset of the above assumptions hold, and this will be presented for a particular example later on in the manuscript.

3. Data and Methods

Inertial motion units (IMUs) equipped with a 3-axis accelerometer, a 3-axis gyroscope, and a 3-axis magnetometer, were used to measure ice motion. The IMUs used are the VN-100 manufactured by VectorNav (2014). Each IMU is factory calibrated for temperatures ranging from -40° to 85°C. The accelerometer has a factory rated resolution of $5 \times 10^{-4} g$ and the angular rate resolution is 3.5×10^{-4} rad s^{-1}. Details of the IMUs and the processing can be found in Rabault et al. (2016).

The VN-100 samples internally at a rate of 800 Hz, and the raw signal is then low-pass filtered by the embedded processor so that the output rate is reduced to 10 Hz. The use of a low-pass filter effectively suppresses aliasing, and reduces the noise level of the instrument. The power spectral density (PSD) was calculated for segments of 45 minutes using the Welch method with a Hanning window of length 5.5 minutes and a half-width overlap. For overlapping segmented data, the degrees of freedom (DoF) can be approximated by (Earle 1996)

$$\mathrm{DoF} = \frac{2K}{1+0.4\,(1-K^{-1})}, \tag{20}$$

where K is the total number of segments. We have 15 segments which give us nearly 22 DoF. The PSD of the acceleration is related to the PSD of the surface elevation by the weighting function ω^{-4} (Tucker and Pitt 2001).

Several steps are outlined to obtain the orthogonal coordinates, i.e. x, y and z, relative to the wave. First, the vertical z axis is obtained by the mean acceleration vector measured by the IMU over the duration of the observations. This assumes that gravity is much greater than any mean inertial accelerations experienced by the IMU. Second, the x direction is obtained by maximizing the variance in the horizontal acceleration, as measured by the IMU, in the orthogonal x-y plane about the z axis. The x direction is then verified by ensuring that the gyroscope also has a maximum variance in the same direction. If the direction is changing in time, then the coordinates could be calculated on time windows comparable to the 45 minute time series used for the PSD estimates.

In our analysis we use three different test cases from two different field studies. The first two cases are from a study performed on fast ice in Tempelfjorden, Svalbard ($78°23'$N, $16°54'$E) during March 2015, as presented in Sutherland and Rabault (2016) and Rabault et al. (2016). The third case is from study on an ice floe in the Barents Sea ($77°45'$N, $25°15'$E) during May 2016. The IMU used for observing the wave motion is identical in each case, while the data acquisition system and configuration has been updated in case c), identical to that presented in Rabault et al. (2017). The ice floe in the Barents sea is approximately 2 km in diameter and 0.3 m thick.

The three different cases all have similar integrated energy, but differ in their frequency distribution. The cases are: a) a mixed sea in Tempelfjorden in fast ice with high frequency energy and an observed deviation from the deep water dispersion relation (Sutherland and Rabault 2016), b) also in Tempelfjorden but after period a) when there was no longer clear evidence for flexural motion and c) a swell dominated regime on a 2km ice floe in the Barents sea. Figure 2 shows the PSD for each of the three cases. A summary of the wave parameters such as significant wave height

H_S, peak period T_p and zero-upcrossing period T_{z0} can be found in Table 1. The significant wave height and zero-upcrossing periods are calculated from the wave moments, i.e. $H_S = 4\sqrt{m_0}$ and $T_{z0} = \sqrt{m_2/m_0}$, where the ith wave moment is defined as

$$m_i = \int_{f_1}^{f_2} f^i S(f) df, \tag{21}$$

where $S(f)$ denotes the PSD and f_1 and f_2 are the frequency limits, which we select to be $f_1 = 0.05$ Hz and $f_2 = 0.25$ Hz. The lower frequency limit is determined by the IMU sensitivity and the upper limit is selected to limit high frequency motion unrelated to surface waves.

In our analysis we will take advantage that the vertical and horizontal acceleration, where the horizontal acceleration is due to the aliasing of the gravity vector, are 90° out of phase and calculate the wave propagation using a rotary spectrum. This technique is commonly used in calculating the rotation of ocean currents (e.g. Gonella 1972), but not so common for surface wave propagation (Sutherland and Rabault 2016).

The vertical and horizontal acceleration measured by the IMU may be written using complex notation, i.e.

$$Z_S(t) + iX_S(t) = a_+ e^{i\omega t} + a_- e^{-i\omega t}, \tag{22}$$

where a_+ is the acceleration in the positive orientation in the $x-z$ plane and a_- is the acceleration in the negative orientation in the $x-z$ plane. Taking the PSD of (22), and scaled by ω^{-4} to convert from acceleration to elevation, gives the energy in the positive (or forward) direction for positive frequencies and the negative (or backwards) direction for negative frequencies. Using the measured accelerations, the energy calculated from the rotary PSD is twice the true value calculated from Z_S. The factor of 2 arises from Z_S and X_S having the same magnitude, which is equal to $a\omega^2$, so the $PSD(Z_S + iX_S) \propto a^2\omega^4 + a^2\omega^4 = 2a^2\omega^4$ where a is the amplitude in equations (17)-(19).

The rotary spectrum is also used to calculate the predominant direction of wave propagation. After the vertical vector is determined from the mean acceleration, which should be equal to g, the two orthogonal vectors are rotated around this z axis and the optimal orientation is chosen by maximizing the integrated energy for the positive frequencies. Figure 3 shows the rotary spectra calculated in the along-wave (blue) and cross-wave (red) direction for the three test cases. Each case has a high asymmetry in the along-wave direction (i.e. any reflected energy is significantly less than the propagating energy) and a high symmetry in the cross-wave direction (i.e. symmetric wave shape).

4. Wave Motion

Investigating the relationship between the accelerations and angles measured by the IMU can shed some light on some of the assumptions that we have made. For example, if $X_S \approx g\theta$ and the magnitudes of X_S and $Z_S - g$ (henceforth the $-g$ is dropped from the notation) are nearly the same, then the assumption of negligible horizontal motion of the ice, small wave steepness and a dispersion relation of $\omega^2 = gk$ are validated. Figure 4 shows the vertical acceleration Z_S and the horizontal acceleration in the direction of wave propagation X_S measured by the IMU, in addition to g times the pitch angle θ. It is clear that $X_S \approx g\theta$ and that any physical horizontal motion in the three cases is negligible. The accelerations X_S and Z_S are similar in magnitude, but not identical. Since the horizontal motion of the ice floe is shown to be negligible, differences between X_S and Z_S will arise from the dispersion relation or possibly from the long-crested approximation.

From (17) and (19), the accelerations Z_S and X_S are expected to be 90 degrees out of phase with one another, which can be tested by looking at the co-spectral density of the two signals. The phase angle, α, between the acceleration measured in the z and x axis can be determined from the co-spectral power density S_{zx}

$$\alpha = \tan^{-1}\left[\frac{\Im\left(S_{zx}\right)}{\Re\left(S_{zx}\right)}\right], \tag{23}$$

where $\Im$ denotes the imaginary part, assuming that the two signals are correlated. The spectral coherence between the two signals, γ_{zx}, is calculated by

$$\gamma_{zx}^2 = \frac{S_{zx}S_{zx}^*}{S_{zz}S_{xx}}, \tag{24}$$

where * denotes the complex conjugate. A value of $\gamma^2 > 0.305$ rejects the hypothesis that the two signals are not correlated at the 99.9% confidence interval (Amos and Koopmans 1963).

The coherence (γ^2) and phase angle (α) between Z_S and X_S are shown in Figure 5 for the three cases. When $\alpha = 90°$, the vertical and horizontal components are in quadrature and the deepwater dispersion relation is valid. The three cases show a slightly different relation between the two orthogonal accelerations. Figures 5b and 5c show that frequencies with a high correlation ($\gamma^2 > 0.75$) correspond with $\alpha \approx 90°$. This is in contrast with Figures 5a and 5b, which both show deviations from $\alpha = 90°$ when coherence is high ($\gamma^2 > 0.75$). This deviation may be due to flexural motions as it increases with frequency, hence $k\ell_c$ has increased. The deviation is greater for case a) than b), which corresponds to a time where there was evidence of flexural motion from the observed dispersion relation (Sutherland and Rabault 2016).

To test the long-crested wave hypothesis, the same analysis was applied to the cross-wave component, Y_S, and in general Y_S and Z_S are not correlated at the 99.9% confidence level. The details of this analysis can be found in the Appendix. This suggests that the phase difference observed between X_S and Z_S is due to the dispersion relation.

5. Directional Spectra

An important aspect of geophysical surface waves is the directional spectrum, which includes information about the direction of wave propagation and the directional spread. The directional spectrum F of surface waves as a function of frequency f and direction ψ can be written as

$$F(f,\psi) = S(f)D(f,\psi), \tag{25}$$

where $S(f)$ is the PSD and $D(f,\psi)$ is a spreading function, which is normalized so that

$$\int_{-\pi}^{\pi} D(f,\psi)d\psi = 1.$$

Longuet-Higgins et al. (1963) showed for a heave, pitch, roll buoy that the directional spectrum can be approximated from the first five Fourier coefficients such that

$$F(f,\psi) = \frac{1}{2}A_0 + (A_1\cos\psi + B_1\sin\psi) + (A_2\cos 2\psi + B_2\sin 2\psi) + \ldots, \tag{26}$$

where the coefficients are determined from the co- C_{ij} and quad- Q_{ij} spectra of the i and j quantities denoted by 1, 2 and 3 for the vertical acceleration, pitch and roll, i.e.

$$\begin{aligned}
A_0 &= \int_{-\pi}^{\pi} F(f,\psi)d\psi = \frac{1}{\omega^4\pi}C_{11} \\
A_1 &= \int_{-\pi}^{\pi} \cos(\psi)F(f,\psi)d\psi = \frac{Q_{12}}{\omega^2\pi}\left(\frac{C_{11}}{C_{22}+C_{33}}\right)^{1/2} \\
B_1 &= \int_{-\pi}^{\pi} \sin(\psi)F(f,\psi)d\psi = \frac{Q_{13}}{\omega^2\pi}\left(\frac{C_{11}}{C_{22}+C_{33}}\right)^{1/2} \\
A_2 &= \int_{-\pi}^{\pi} \cos(2\psi)F(f,\psi)d\psi = \frac{C_{22}-C_{33}}{\pi}\left(\frac{C_{11}}{C_{22}+C_{33}}\right) \\
B_2 &= \int_{-\pi}^{\pi} \sin(2\psi)F(f,\psi)d\psi = \frac{C_{23}}{\pi}\left(\frac{C_{11}}{C_{22}+C_{33}}\right).
\end{aligned} \tag{27}$$

Longuet-Higgins et al. (1963) went on to show that omitting the higher order terms in (26) is equivalent to applying a weighting function to the true spectrum, i.e.

$$F_1(f,\psi) = \frac{1}{2\pi}\int_{-\pi}^{\pi} F(f,\psi')W_1(\psi'-\psi)d\psi', \tag{28}$$

where $W_1 = 1 + 2\cos(\psi' - \psi) + 2\cos 2(\psi' - \psi)$ and F_1 is the truncated (26). The weighting function W_1 can be negative for certain directions, which can make $F_1(f,\psi)$ negative while $F(f,\psi)$ is expected to be strictly positive. To avoid negative energy, Longuet-Higgins et al. (1963) proposed an alternate weighting function which is positive for all directions, but arbitrarily widens the distribution,

$$F_2(f,\psi) = \frac{1}{2}A_0 + \frac{2}{3}(A_1\cos\psi + B_1\sin\psi) + \frac{1}{6}(A_2\cos 2\psi + B_2\sin 2\psi). \tag{29}$$

Figure 6 shows the directional distribution, where $D_i(f,\psi) = F_i(f,\psi)/S(f)$, at the peak frequency for each test case. The truncated Fourier series, $D_1(f,\psi)$, gives a narrower peak, negative energy around $\pm 90°$ and positive energy at $\pm 180°$ from the direction of propagation. This is quite different than for $D_2(f,\psi)$ which smooths out the spectral energy to angles greater than $\pm 90°$ and does not have a second peak at $\pm 180°$. So, while it is true that $D_1(f,\psi)$ is negative at directions that are orthogonal to the principal direction of propagation, most of the energy for waves in ice are expected to be along one principal direction (Wadhams et al. 1986). Furthermore, since the slope is generally very small for waves in ice, the curvature will be significantly smaller allowing for a further argument for using the truncated Fourier series as opposed to selecting somewhat arbitrary weights.

In order to compare the directional spectra estimates with the rotary spectra method, the directional spectra is integrated over each hemisphere as

$$\begin{aligned} S_{Di}(f) &= \int_{-\pi/2}^{\pi/2} \cos\psi F_i(f,\psi)\, d\psi \\ S_{Di}(-f) &= \int_{-\pi/2}^{\pi/2} |\cos(\psi - \pi)| F_i(f,\psi - \pi)\, d\psi, \end{aligned} \tag{30}$$

where i is either 1 or 2 depending on which directional form is used for the wave spectra. The cosine term in (30) is used to project the directional spectra on the axis of propagation used for the rotary spectra. While cosine weighting has little effect on the positive frequencies as most of the energy is at $\psi = 0$, it will impact the negative frequencies where energy at $\psi = \pm 90^\circ$ can be comparable to $\psi = \pm 180^\circ$ depending on the spreading function used. Figure 7 shows the comparison of (30) with estimates using the 1-D vertical, 1-D horizontal and rotary spectra. Note the lower noise level of case c) compared with the other two cases. This is due to the implementation of the onboard low-pass filter for the Lance cruise, which was not done with the setup for the Tempelfjorden experiment. The onboard filter is programmed to obtain a boxcar average of 80 adjacent samples at the internal IMU sampling rate of 800 Hz and outputs this value at 10 Hz.

There is good qualitative agreement between all estimates of the PSD for the three test cases presented. It is somewhat surprising/encouraging that there is such excellent agreement for the negative frequencies, i.e. the "reflected" energy portion of the spectra, and that both directional spectral shape give similar estimates. This result suggests that the reflection coefficient may be independent of the exact shape of the distribution and calculated from integrated parameters, similar to directional spread (Kuik et al. 1988).

a. Comparisons with Rotary Spectra

The rotary spectra of the counter-clockwise and clockwise rotating components (which we will denote by positive and negative frequencies) can be written in terms of the co- and quad-spectra of the two components (Gonella 1972), i.e.

$$S_{xz}^{\mathrm{rot}}(f) = \frac{1}{8}\left(C_{xx} + C_{zz} + 2Q_{xz}\right) \tag{31}$$

$$S_{xz}^{\mathrm{rot}}(-f) = \frac{1}{8}\left(C_{xx} + C_{zz} - 2Q_{xz}\right), \tag{32}$$

where C_{ij} and Q_{ij} are the co- and quad-spectra used to define the Fourier coefficients in (27). Noting that z is equivalent with 1 in (27) and x is equivalent with g times 2 in (27), and using the deep water dispersion relation (i.e. $C_{zz} = C_{xx}$), which assumes that the wavenumber k satisfies both $(k\ell_c)^4 \ll 1$ and $\tanh kH \approx 1$, we obtain (31) and (32) in terms of the Fourier coefficients, i.e.

$$S_{xz}^{\mathrm{rot}}(f) = \frac{A_0 \pi \omega^4}{4}\left(1 + \frac{A_1}{A_0}\right) \tag{33}$$

$$S_{xz}^{\mathrm{rot}}(-f) = \frac{A_0 \pi \omega^4}{4}\left(1 - \frac{A_1}{A_0}\right). \tag{34}$$

Similarly, the rotary spectra in the cross-wave direction can be written as

$$S_{yz}^{\mathrm{rot}}(f) = \frac{A_0 \pi \omega^4}{4}\left[\left(\frac{1}{2} + \varepsilon^2\right) + \frac{B_1}{A_0}\right] \tag{35}$$

$$S_{yz}^{\mathrm{rot}}(-f) = \frac{A_0 \pi \omega^4}{4}\left[\left(\frac{1}{2} + \varepsilon^2\right) - \frac{B_1}{A_0}\right]. \tag{36}$$

Equations (33)-(36) will be used to infer calculated values of directional spread and reflection with the Fourier coefficients.

b. Wave Reflection

Estimating wave reflection in an ice-covered sea is difficult as it requires the ability to resolve a bimodal spectrum, with the modes 180° apart, which is challenging using traditional techniques (Benoit 1992). A classic option is to statistically fit a parametric model for spreading from the data, a common model is the "cosine-2s model" $D(\psi) \propto \cos^{2s}(\psi/2)$ where s is the spreading factor, and is identical to the methodology of Wadhams et al. (1986) in their study of directional spectra in sea ice. While such methods have shown to be effective in open water (Benoit 1992), there is little evidence suggesting that they will be as effective under an ice cover. Instead, we propose a simple method using rotary spectra, which can determine wave propagation by the clockwise and counter-clockwise components. This method may be particularly well suited to measure waves in ice as IMUs follow the surface relatively well with little horizontal acceleration (see Figure 4). Furthermore, Wadhams et al. (1986) showed in their analysis that the direction of the reflected spectral peak is very close to 180° from the direction of the incident wave, which is an ideal situation for the use of rotary spectra.

Figure 7 shows that estimates of the reflected energy using the rotary spectra are similar to the directional spectra estimates projected onto the negative along-wave axis. It is expected that the shape of the directional spectrum $D(f,\psi)$ would affect the estimate of the reflected energy, but Figure 7 shows very similar estimates using the two different directional shapes. In Figure 6, $D_1(f,\psi)$ shows two separate peaks at $\psi = 0°$ and $\psi \approx \pm 180°$ while $D_2(f,\psi)$ shows a broad peak which extends to angles greater than 90° and goes to zero for $\psi = \pm 180°$. While the two directional estimates are quite different in the directional distribution of energy, it is striking that the integrated values are similar and that the energy propagating from the sea and towards the sea are consistent between the two methods.

The reflection coefficient R^2 is calculated from Figure 7 using the definition

$$R^2 = \frac{S(-f)}{S(f)}, \tag{37}$$

where $S(\pm f)$ is the PSD estimated using either of the rotary spectral or directional spectral methods, $-f$ denotes the frequency of the reflected energy and f is the frequency of the propagating energy. The reflection coefficient can also be written in terms of the Fourier coefficients using (33) and (34), which becomes

$$R_F^2 = \frac{1 - A_1/A_0}{1 + A_1/A_0}. \tag{38}$$

Figure 8 shows R^2 estimated using the different methods for the three cases. In all three cases, R_{D2}^2 is greater than the other estimates, which we interpret to arise from the increased spread due to the smoothing function as the weighting function is 0 when $\psi = \pm\pi$. The other estimates produce a striking similarity with one another. This similarity suggests that (38) may provide a model-free estimate of the reflection coefficient that can be calculated from the first order Fourier coefficients.

c. Directional Spread

Another important aspect is the directional spread of the propagating wave field. This term is model independent as it can be calculated from the first order Fourier coefficients (Kuik et al. 1988), i.e.

$$\sigma_1 = \sqrt{2\left(1-\frac{C_1}{A_0}\right)} \tag{39}$$

$$\sigma_2 = \sqrt{\frac{1}{2}\left(1-\frac{C_2}{A_0}\right)}, \tag{40}$$

where $C_i = \sqrt{A_i^2 + B_i^2}$. Equation (40) deviates slightly from the definition of Kuik et al. (1988) by using a different definition for C_2. Our definition for σ_2 is consistent with Ardhuin et al. (2016), and is chosen as it is solely dependent on the second order Fourier coefficients. While not shown here, the difference between the two definitions of σ_2 is minimal.

We propose that the directional spread may also be estimated from the rotary spectra in the along- and cross-wave directions, which we define as

$$\sigma_r(f) = \tan^{-1}\left[\frac{S_{yz}^{\mathrm{rot}}(f)}{S_{xz}^{\mathrm{rot}}(f)}\right] + \tan^{-1}\left[\frac{S_{yz}^{\mathrm{rot}}(-f)}{S_{xz}^{\mathrm{rot}}(f)}\right], \tag{41}$$

where S_{xz}^{rot} is the along-wave (i.e. $x-z$ plane) rotary spectra and S_{yz}^{rot} is the cross-wave (i.e. $y-z$ plane) rotary spectra. Equation (41) gives a clear geometric relation between the along-wave and cross-wave direction for each frequency. The spread calculated by (41) can also be estimated from the Fourier coefficients using (33)-(36), i.e.

$$\sigma_r^*(f) = \tan^{-1}\left[\frac{0.5+B_1/A_0}{1+A_1/A_0}\right] + \tan^{-1}\left[\frac{0.5-B_1/A_0}{1+A_1/A_0}\right], \tag{42}$$

where ε is neglected and thus σ_r^* is expected to provide a lower-bound on the estimated spread.

Another method for the determination of the directional spread is to calculate the root-mean-square spread (Kuik et al. 1988), i.e.

$$\sigma_D = \sqrt{\int_{-\pi}^{\pi} (\psi - \psi_0)^2 D(f,\psi) d\psi}, \tag{43}$$

where ψ_0 is the mean wave direction defined from the Fourier coefficients as $\psi_0 = \tan^{-1} B_1/A_1$. There are various drawbacks to using (43), such as it requires calculating the directional distribution $D(f,\psi)$ and is not expected to be valid for large spreads (Longuet-Higgins et al. 1963), but it is presented here for purely comparative purposes.

Equation (41) estimates the spread from a purely geometrical reasoning, and thus the isotropic limit of $\sigma_r^{iso} = \pi/2 = 90°$ is more intuitive than previous estimates. For example, the isotropic limit of (39) is $\sigma_1^{\text{iso}} = \sqrt{2} \approx 81°$ while for (40) it is $\sigma_2^{\text{iso}} = \sqrt{2}/2 \approx 40.5°$. Furthermore, the isotropic limit of (43) is $\sigma_D^{\text{iso}} = \pi/\sqrt{3} \approx 104°$. It is tempting to normalize each estimate of spread by a factor related to the isotropic limits (see Squire and Montiel 2016). However, this is inconsistent with the results of Kuik et al. (1988), which showed that σ_1, σ_2 and σ_D all give similar results using synthetic data with relatively narrow angular distributions. It is hard to know a priori if the spread will be small or not so we scale each spread in a similar way as Squire and Montiel (2016), but in our case we scale them to all have the isotropic limit of 90°.

Figure 9 shows the comparison between the various definitions for the spread for the three test cases. Equation (42) assumes $\varepsilon = 0$, which will give a lower estimate to the directional spread. For frequencies less than 0.15 Hz, all estimates of the spread, with the exception of σ_{D2}, give strikingly similar results. It is not too surprising that σ_{D2} is a bit larger as the directional spectrum is arbitrarily widened by a smoothing function in order to ensure the energy is positive for all angles.

There are some subtle differences between the methodologies. For instance, in Figure 9a there is a deviation of spread estimates at $f = 0.15$ Hz, which coincides to the frequency where a change in the dispersion relation due to flexural motions was observed (Sutherland and Rabault 2016). After this transition frequency the estimates converge for frequencies greater than 0.17 Hz suggesting that the effect of flexural motions on the calculated spread is complicated. This complication is also present in Figure 9b where spread estimates also deviated for frequencies between 0.17 and 0.20 Hz. For case c) (Figure 9c) the spread is consistent between the scaled estimates, with the exception of σ_{D1} for the same reasons as mentioned in the previous paragraph.

6. Summary and Discussion

A new method for calculating aspects of directional wave spectra, such as mean direction, spread, and reflection is presented for a single inertial motion unit (IMU) mounted on sea ice. This method is based on calculating the rotary spectra of the vertical and horizontal components of the acceleration as measured in the IMU reference, where the horizontal acceleration has been shown to be equal to g times the slope. This measured horizontal acceleration is predominantly due to the projection of the gravity vector on the horizontal axis due to the sloping surface and any physical horizontal motion is negligible. While this is the case for our data, where the ice floe is much larger than the wavelength, it remains to be seen if the same relation will hold for IMUs on much smaller floes. For example, Fox and Haskell (2001) observed negligible horizontal acceleration on ice floes of approximately 7 m to 9 m in diameter. As these floes are much smaller than their range of observed wavelength of approximately 50 m to several hundred metres, the floes are expected to follow the orbital motion of the waves. Therefore, the physical acceleration due to the orbital motion may cancel the aliasing of the gravity vector due to the surface slope as it is expected to be equal in magnitude and opposite in sign as shown in (17)-(19).

Since the horizontal acceleration is shown to be equivalent to the slope, we presented a method to estimate the reflection and directional spread using a rotary spectra technique (Gonella 1972). The rotary spectra method is compared with directional estimates obtained using the method of Longuet-Higgins et al. (1963) using different weighting functions. The first weighting function is using the truncated Fourier series, which assumes that the effects from the higher order spectra are negligible, but can give negative energy at angles around $\pm 90°$ from the principal direction of propagation. The second weighting function is the one presented by Longuet-Higgins et al. (1963), which arbitrarily widens the spectra but has the advantage of ensuring that the directional spectral energy is positive for all directions. Although both methods have different spectral shapes, they are both found to be consistent with the rotary spectra when projected onto the axis of propagation and integrated over each hemisphere, i.e. $-\pi/2 < \psi < \pi/2$ for the propagating wave and $-\pi/2 < \psi - \pi < \pi/2$ for the reflected component. This result suggests that the difference between the two weighting functions are minimal for such a coarse directional resolution.

Our examples consisted of unimodal or bimodal seas where the modes are about $180°$ apart, and the rotary spectrum is naturally suited for such scenarios, but in more complicated multi-modal seas then it is likely that the method may not perform as well. For instance, since the principal direction is determined from the time series by locating the direction which maximizes the along-wave variance, this will find the mean direction associated with the peak of the wave spectra, and not for each frequency band. It may be possible to devise a metric of "multi-modalness", which investigates the symmetry in the cross-wave direction and asymmetry in the along-wave direction as our observations (Fig. 3) suggest this to be the case for our predominantly unimodal or bimodal seas. Our comment on this is primarily speculation as our data does not contain such complicated wave fields. Further research is required to investigate the possibility of extending our method to multi-modal seas.

The reflection coefficient is calculated using both the rotary spectra and the estimated directional spectra. The calculated reflection coefficients are similar for the three cases using the two methods, with the wider directional distribution D_2 giving slightly larger values, presumably from the spread of energy to angles greater than $90°$ from the principal direction of propagation. A derivation for the reflection coefficient is presented which is model-independent in that it can directly be calculated from the Fourier coefficients. This model independent reflection coefficient compares favourably with the estimates other than D_2, especially when the directional spread is small, i.e. near the spectral peak.

Estimates of the directional spread using rotary spectra compared well with the model-independent estimates of Kuik et al. (1988) when proper scaling factors were applied to give the same isotropic limit. The isotropic limit using rotary spectra is $\sigma_r = \pi/2 = 90°$, while the isotropic limits for the other methods are $\sigma_1 = \sqrt{2} \approx 81°$, $\sigma_2 = \sqrt{2}/2 \approx 41°$, and the rms deviation $\sigma_D = \pi/\sqrt{3} \approx 104°$. While it is expected that $\sigma_1 = \sigma_2 = \sigma_D$ for small directional spreads (Kuik et al. 1988), we found the isotropic scaling to be necessary for the estimates to be consistent in our data. This type of scaling, based on the isotropic limit, was also employed by Squire and Montiel (2016) in order to relate the spread estimates of the marginal ice zone model of Montiel et al. (2016) with the field observations of Wadhams et al. (1986). In addition, our observations of wave spreading near the peak frequency were consistently around $30°$, which is similar to the spread calculated by Wadhams et al. (1986) in the marginal ice zone. It is not clear to us why scaling the directional spread by the isotropic limits gives consistent results between the various methods as near the spectral peak the directional spreads are much less than the isotropic limit and our previous analysis (section 4) suggests that the wave propagation is predominantly in one direction. This is somewhat troubling that different methodologies give such different results and care must be taken when using measurements of directional spread.

Our observations of surface waves under sea ice suggest that the linear accelerations measured in the IMU frame of reference can be related to the angular motion and vice versa in the case of long-crested waves travelling through pack ice (Liu and Mollo-Christensen 1988; Ardhuin et al. 2016). This simplifies the sensors necessary to measure the directional aspects of surface waves, which could lead to a further reduction in cost, both in terms of number of sensors and amount of data that needs to be recorded and/or transmitted. In situations where the horizontal acceleration is not negligible, the rotary method may still be valid as long as additional data is recorded. For example, the angle about the three orthogonal axes and the floe response to the incident wave. This difficulty suggests that a multi-sensor approach will be necessary to measure the wave field in a variety of sizes and shapes of sea ice.

Acknowledgments. The authors are grateful to Aleksey Marchenko for his help with the field work in Tempelfjorden and during the Lance Cruise. We also thank Brian Ward, Kai Christensen, Trygve Halsne, Erika Lindström, and Olav Gunderson for their help during the Tempelfjorden study and Benjamin Hergoualc'h for his work deploying the sensors during the Lance study. Funding for the experiment was provided by the Norwegian Research Council under the PETRO-MAKS2 scheme [Grant Number 233901]. The data is available from the corresponding author upon request.

APPENDIX

Cross-wave coherence

In addition to the along-wave propagation, the propagation in the cross-wave direction is also investigated. Figure A1 shows that the acceleration and the cross-wave slope follow each other reasonably well for all three cases, with the best agreement occurring for case c). The vertical acceleration is scaled by 0.3 for visualization purposes.

In the same manner for the along-wave, the coherence and phase difference is calculated for the vertical and horizontal motion in the cross-wave direction and is shown in Figure A2. The coherence is much smaller than for the along-wave motion with only case a) showing coherence at the 99.9% confidence interval. This is in contrast with equations (18) and (19), which suggests that physical motions and/or noise are present which are at least similar in magnitude to the aliased gravity vector due to the cross-wave slope.

References

Amos, D., and L. Koopmans, 1963: *Tables of the distribution of the coeffient of coherence for stationary bivariate Gaussian processes*. Sandia Corp., Albuquerque, N. Mex.

Ardhuin, F., P. Sutherland, M. Doble, and P. Wadhams, 2016: Ocean waves across the arctic: attenuation due to dissipation dominates over scattering for periods longer than 19 s. *Geophys. Res. Lett.*, **43**, doi:10.1002/2016GL068204.

Bender III, L., N. Guinasso Jr, J. Walpert, and S. Howden, 2010: A comparison of methods for determining significant wave heights-applied to a 3-m discus buoy during hurricane katrina. *J. Atmos. Oceanic Technol.*, **27 (6)**, 1012–1028.

Benoit, M., 1992: Practical comparative performance survey of methods used for estimating directional wave spectra from heave-pitch-roll data. *Proc. 23rd ICCE*, ASCE, Vol. 1, 62–75.

Doble, M. J., and P. Wadhams, 2006: Dynamical contrasts between pancake and pack ice, investigated with a drifting buoy array. *J. Geophys. Res. Oceans*, **111 (C11)**.

Earle, M. D., 1996: Nondirectional and directional wave data analysis procedures. *NDBC Tech. Doc*, 96–01.

Fox, C., and T. G. Haskell, 2001: Ocean wave speed in the Antarctic marginal ice zone. *Ann. Glaciol.*, **33 (1)**, 350–354.

Fox, C., T. G. Haskell, and H. Chung, 2001: Dynamic, in situ measurement of sea-ice characteristic length. *Ann. Glaciol.*, **33 (1)**, 339–344.

Gonella, J., 1972: A rotary-component method for analysing meteorological and oceanographic vector time series. *Deep-Sea Res.*, Vol. 19, 833–846.

Kohout, A. L., B. Penrose, S. Penrose, and M. J. M. Williams, 2015: A device for measuring wave-induced motion of ice floes in the Antarctic marginal ice zone. *Ann. Glaciol.*, **56 (69)**, 415–424.

Kuik, A., G. P. Van Vledder, and L. Holthuijsen, 1988: A method for the routine analysis of pitch-and-roll buoy wave data. *J. Phys. Oceanogr.*, **18 (7)**, 1020–1034.

Lawson, L. M., and R. B. Long, 1983: Multi-modal properties of the surface wave field observed with pitch-roll buoys during GATE. *J. Phys. Oceanogr.*, **10**, 944–952.

Liu, A. K., and E. Mollo-Christensen, 1988: Wave propagation in a solid ice pack. *J. Phys. Oceanogr.*, **18 (11)**, 1702–1712.

Long, R. B., and K. Hasselmann, 1979: A variational technique for extracting directional spectra from multi-modal wave data. *J. Phys. Oceanogr.*, **9**, 373–381.

Longuet-Higgins, M. S., D. Cartwright, and N. Smith, 1963: Observations of the directional spectrum of sea waves using the motions of a floating buoy. *Ocean Wave Spectra*, Prentice-Hall, 111–136.

Marchenko, A., 1999: The floating behaviour of a small body acted upon by a surface wave. *J. Appl. Math. Mech.*, **63 (3)**, 471–478.

Marchenko, A., E. Morozov, and S. Muzylev, 2013: Measurements of sea-ice flexural stiffness by pressure characteristics of flexural-gravity waves. *Ann. Glaciol.*, **54 (64)**, 51–60.

Masson, D., and P. LeBlond, 1989: Spectral evolution of wind-generated surface gravity waves in a dispersed ice field. *J. Fluid Mech.*, **202**, 43–81.

Meylan, M., and V. A. Squire, 1994: The response of ice floes to ocean waves. *J. Geophys. Res.*, **99**, 891–891.

Montiel, F., V. Squire, and L. Bennetts, 2016: Attenuation and directional spreading of ocean wave spectra in the marginal ice zone. *J. Fluid Mech.*, **790**, 492–522.

Rabault, J., G. Sutherland, O. Gundersen, and A. Jensen, 2017: Measurements of wave damping by a grease ice slick in svalbard using off-the-shelf sensors and open-source electronics. *J. Glaciol.*, 1–10, doi:10.1017/jog.2017.1.

Rabault, J., G. Sutherland, B. Ward, K. H. Christensen, T. Halsne, and A. Jensen, 2016: Measurements of waves in landfast ice using inertial motion units. *IEEE Trans. Geosci. Remote Sens.*, 1–10, doi:10.1109/TGRS.2016.2584182.

Squire, V., 2007: Of ocean waves and sea-ice revisited. *Cold Reg. Sci. Technol.*, **49 (2)**, 110–133.

Squire, V. A., J. P. Dugan, P. Wadhams, P. J. Rottier, and A. K. Liu, 1995: Of ocean waves and sea ice. *Ann. Rev. Fluid Mech.*, **27 (1)**, 115–168.

Squire, V. A., and F. Montiel, 2016: Evolution of directional wave spectra in the marginal ice zone: a new model tested with legacy data. *J. Phys. Oceanogr.*, **46**, 3121–3137.

Sutherland, G., and J. Rabault, 2016: Observations of wave dispersion and attenuation in landfast ice. *J. Geophys. Res. Oceans*, **121**, 1984–1997, doi:10.1002/2015JC011446.

Tucker, M. J., and E. G. Pitt, 2001: *Waves in ocean engineering*, Vol. 5. Elsevier, 550 pp.

VectorNav, 2014: *VN-100 User Manual*. VectorNav Technologies, version 2.05, 128 pp.

Vindegg, C. M., 2014: Stress measurements in landfast sea ice in van mijenfjorden, svalbard.: A survey of internal stress in landfast sea ice winter 2014. Ph.D. thesis, Norwegian Univ. Sci. Tech., Trondheim, Norway.

Wadhams, P., V. A. Squire, J. A. Ewing, and R. W. Pascal, 1986: The effect of the marginal ice zone on the directional wave spectrum of the ocean. *J. Phys. Oceanogr.*, **16 (2)**, 358–376.

Wadhams, P., V. A. Squire, D. J. Goodman, A. M. Cowan, and S. C. Moore, 1988: The attenuation rates of ocean waves in the marginal ice zone. *J. Geophys. Res. Oceans*, **93 (C6)**, 6799–6818.

Yiew, L., L. Bennetts, M. Meylan, B. French, and G. Thomas, 2016: Hydrodynamic responses of a thin floating disk to regular waves. *Ocean Modelling*, **97**, 52–64.

Young, I., 1994: On the measurement of directional wave spectra. *Appl. Ocean Res.*, **16 (5)**, 283–294.

LIST OF TABLES

TABLE 1. Wave parameters for the three test cases chosen in this study.

Case	H_S (m)	T_p (s)	T_{z0} (s)
a	0.082	7.7	7.9
b	0.088	8.8	8.9
c	0.083	12.8	10.1

LIST OF FIGURES

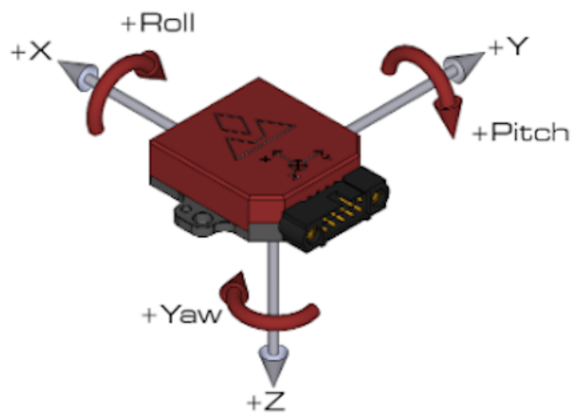

FIG. 1. Axis orientation for the VN-100 IMU.

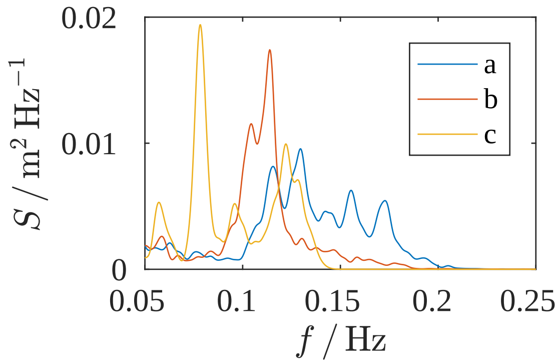

FIG. 2. One dimensional PSD for three test cases.

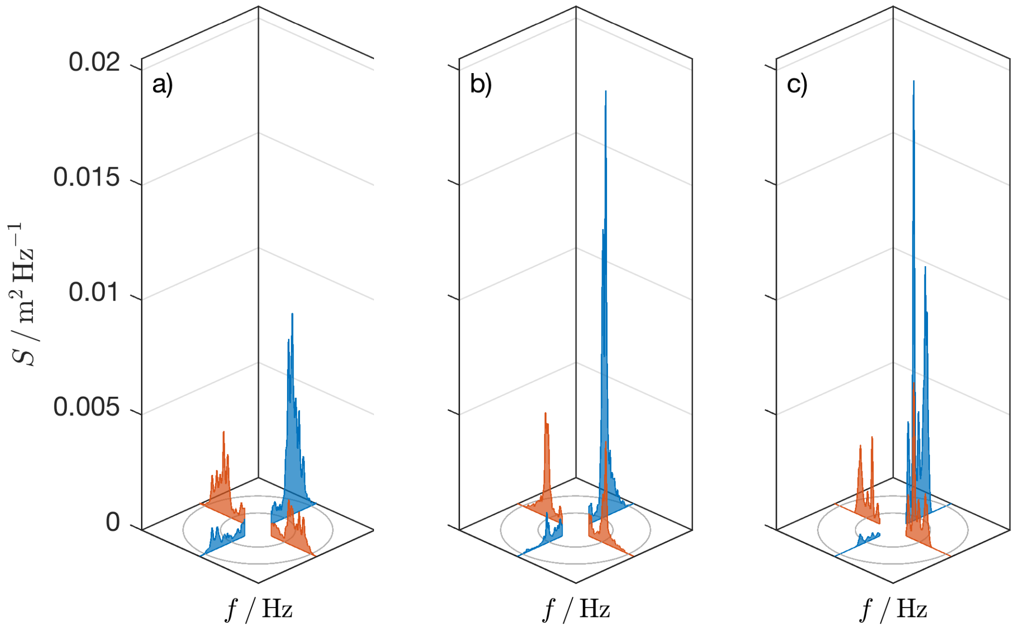

594 FIG. 3. Rotary spectra in the along (blue) and cross (red) directions for the three cases denoted a), b) and c). The grey circles on the base represent 0.1 Hz frequency contours.

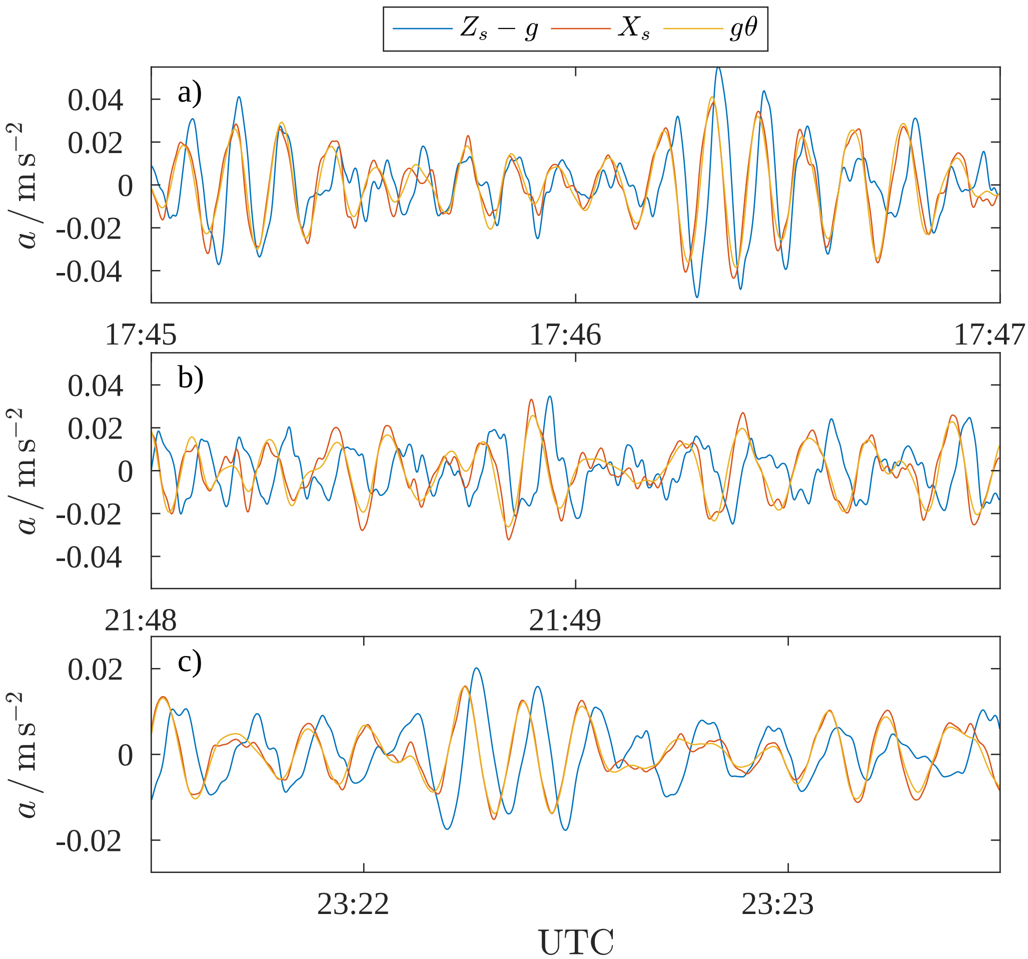

FIG. 4. Acceleration in the along-wave direction measured in the sensor frame of reference for the three cases denoted a), b) and c). The horizontal acceleration is predominantly due to the projection of the gravity vector and is equal to $g\theta$.

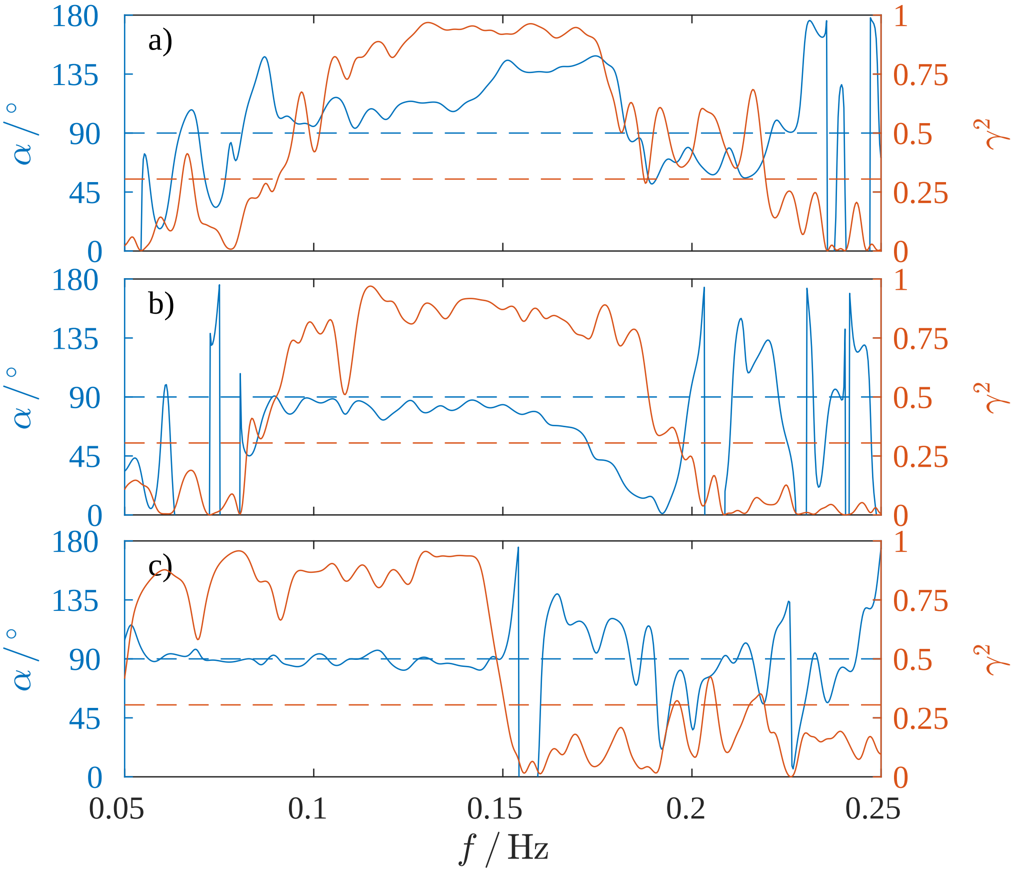

FIG. 5. Phase angle and correlation measured in the sensor frame of reference for the three cases denoted a), b) and c). The blue line shows the phase angle between $Z_S - g$ and X_S with the blue dashed line showing a phase difference of 90°. The red line shows the coherence squared and the red dashed line indicates the 99.9% probability of rejecting the null hypothesis.

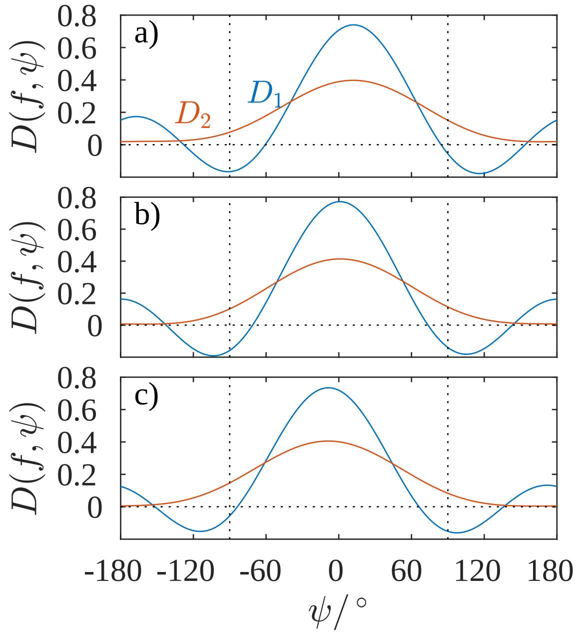

FIG. 6. Directional spreading function of truncated Fourier series D_1 (blue) and weighted function D_2 proposed by Longuet-Higgins et al. (1963) (red) at the peak frequency for the three cases denoted a), b) and c).

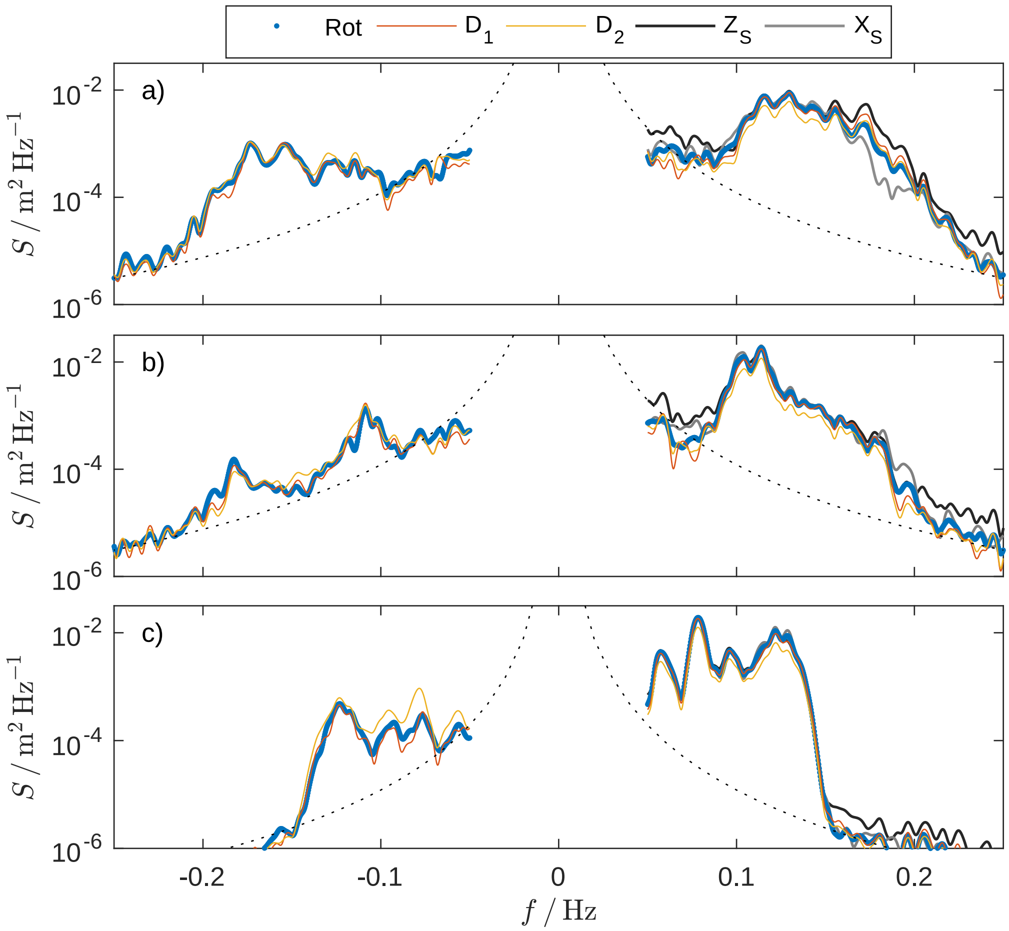

605 FIG. 7. Rotary spectra compared with other spectral energy estimates for the three cases denoted a), b) and
606 c). The noise level is shown by the dashed black line. Note that c) has a lower noise level than a) and b).

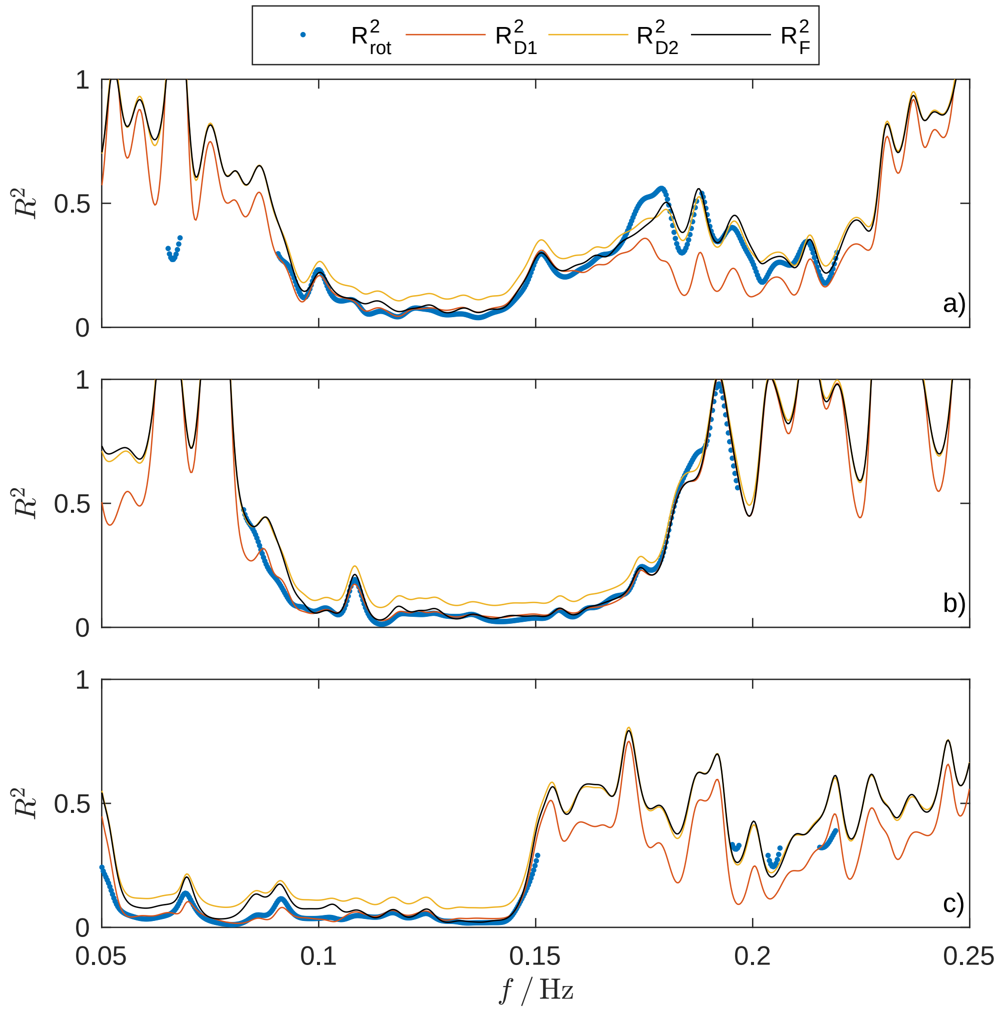

FIG. 8. Comparison of the reflection coefficient for the three cases, denoted a), b) and c), estimated from the rotary spectrum (blue) and the directional spectrum for two different directional spreading functions.

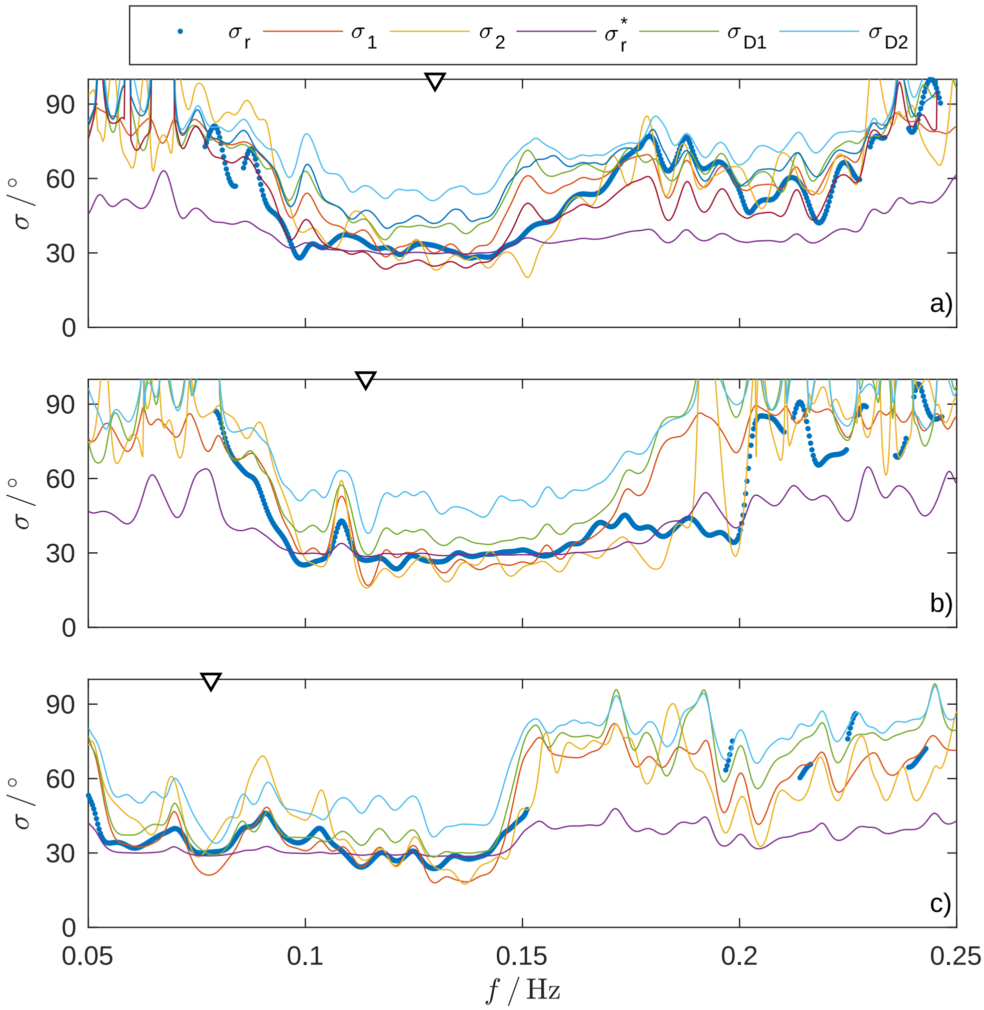

609 FIG. 9. Directional spread measured in the sensor reference frame for the three cases denoted a), b) and c).
610 The inverted triangles show local peaks in the 1-D spectrum. Each estimate of the directional spread is multiplied
611 by a factor to ensure their respective isotropic values are equal to 90°.

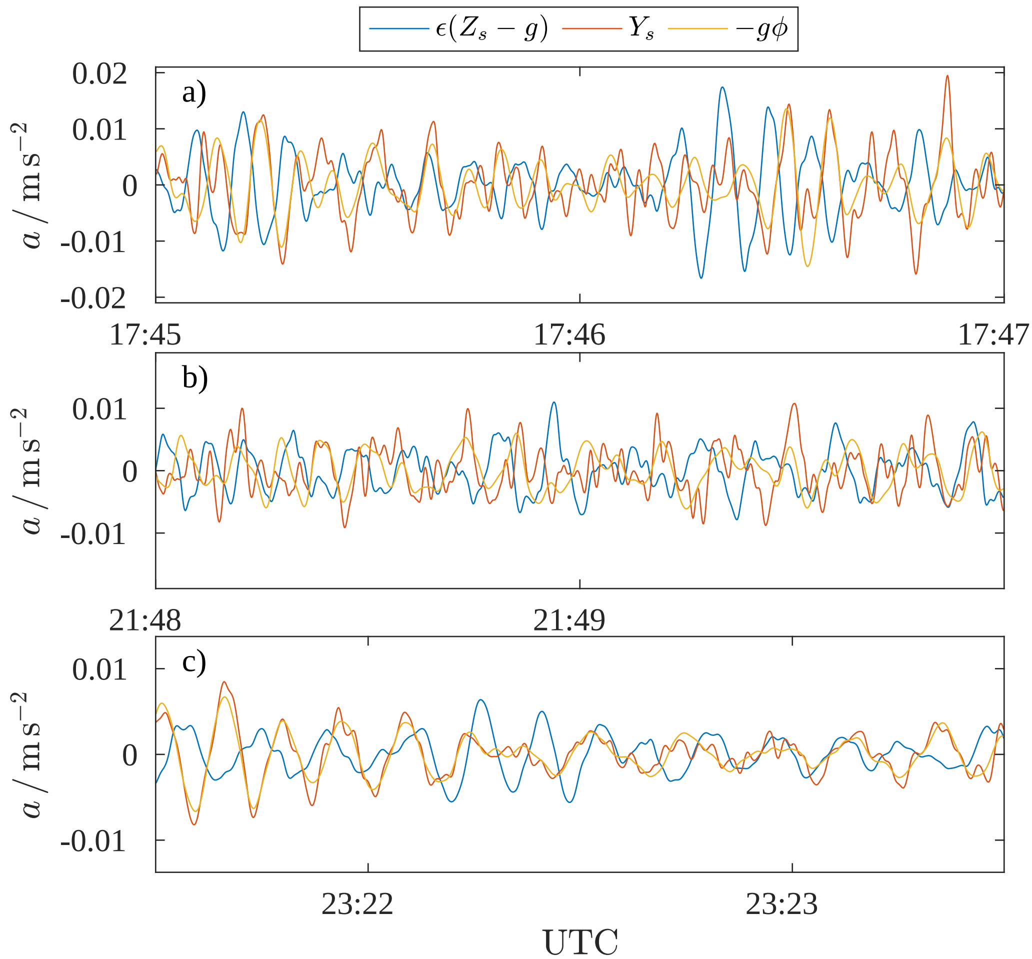

612 Fig. A1. Acceleration in the cross-wave direction measured in the sensor frame of reference for the three cases. The horizontal acceleration measured in the IMU reference frame is predominantly due to the projection of the gravity vector with ε estimated to be about $\sqrt{0.1} \approx 0.3$ for illustrative purposes.

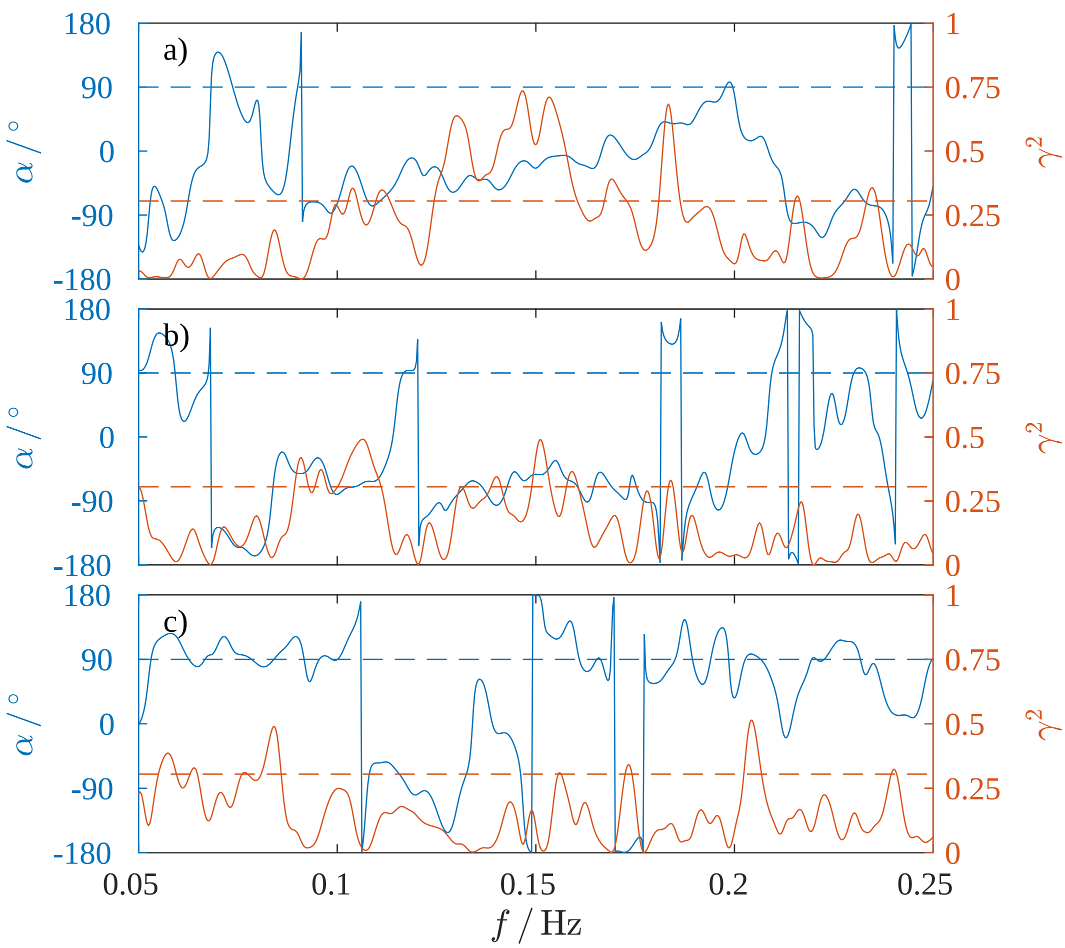

615 Fig. A2. Phase angle and correlation measured in the sensor reference frame for the three cases. The blue
616 line shows the phase angle between $Z_S - g$ and Y_S with the blue dashed line showing a phase difference of 90°.
617 The red line shows the coherence squared and the red dashed line indicates the 99.9% probability of rejecting
618 the null hypothesis.